

might be a too restricting assumption in complex problems typical in high-lift aerodynamics because a multitude of different flow phenomena can be present in a single problem. Therefore, turbulence modeling with a wider range of applicability than the Boussinesq models must be looked for. Reynolds-stress transport modeling (RST), in which a modeled transport equation is solved for each stress component, is in principle a more general class of models with a wider range of applicability. RSTs are, however, considered as a too complex approach for the industrial aerodynamic design work. On the other hand, the two-equation models can be extended for a wider range of applicability by developing more advanced nonlinear constitutive modeling. Explicit algebraic Reynolds-stress models (EARSM) are an interesting subset of nonlinear models. In this approach, part of the higher-order description of physical processes in the RST level is transferred into the two-equation modeling level. The EARSM approach is considered to be a suitable type of constitutive modeling for the present purposes. There are also other kinds of more advanced models than the standard linear two-equation models. Durbin's v^2 - f model¹ is maybe the best known example of such models. In this work, however, the EARSM approach is adopted.

Most of the existing two-equation scale-determining models are designed in conjunction with the linear constitutive modeling. This fact can compromise the performance of the model when combined with an EARSM or another nonlinear constitutive model. The aim of this study was to develop a new k - ω model to be used purely with the EARSM as a constitutive model. The model is designed to be utilized mainly for aerodynamic problems, especially for high-lift aerodynamics. This does not mean that the model is unsuitable for all other flow problems, but the focus is kept in flow phenomena that have an important role in typical high-lift aerodynamics problems. Boundary layers under adverse pressure gradient, wakes, and mixing layers are considered as important elementary flows in the model development. Wakes are very important because the interaction between wakes and boundary layers might be the factor that controls the maximum lift of multielement airfoils.

The development was started from Menter's k - ω model,² and it is completely recalibrated in conjunction with the selected EARSM constitutive model.³ Menter's k - ω model is selected as a starting point because it is one of the most popular and successful turbulence models applicable in practical aerodynamics engineering work to date. Menter's k - ω model has previously been combined with EARSM as a constitutive model, for example, see Refs. 4–6. The resulting model behaves quite much like the original model in simple shear flows, but it has better potential to predict the effects of streamline curvature, swirl, rotation, and other complexities. However, there are also some problems. For instance, the velocity profile in the defect layer of a zero-pressure-gradient boundary layer has a qualitatively wrong shape. This failure in predicting the very elementary flow indicates that the constitutive model cannot necessarily be changed without recalibrating the scale-determining model. Moreover, Menter's models, both the original models and the EARSM versions predict unphysically sharp edges for the turbulent regions, and they predict wakes to spread far too slowly. More or less poor behavior near the outer edges of the turbulent regions has been one of the most significant weaknesses of the k - ω model family. Therefore, much attention is paid on the edge behavior in developing the new model. The analysis first proposed by and Spalart and Allmaras⁷ and more generally derived by Cazalbou et al.,⁸ and later by Catris and Aupoix⁹ and by Kok¹⁰ is extended for models with variable eddy-viscosity coefficient C_μ such as nonlinear eddy-viscosity models and EARSMs.^{11,12} The earlier work assumed constant C_μ and is thus restricted to linear eddy-viscosity modeling. As an exception, the recent work by Cazalbou and Chassaing¹³ extended this analysis to RST models. To the author's knowledge, however, this kind of analysis has not been applied to nonlinear two-equation models by other researchers. The present analysis enforced the recent observation by Hellsten and Bézard¹² that the diffusion coefficient of k needs a stricter limit, namely, $\sigma_k > 1$, when EARSM is used as a constitutive model. With linear constitutive modeling, it is sufficient to have $\sigma_k > 0.5$. It was shown both analytically

and numerically that violation of the new constraint leads to a highly anomalous hook-shaped velocity profile around the outer edge of turbulent region. This fact renders many existing k - ω models unsuitable to be used with EARSM as the constitutive model.¹¹ Wilcox's k - ω models^{14,15} and Kok's k - ω turbulent/nonturbulent (TNT) model¹⁰ can be mentioned as examples of such models.

This paper presents a summary of the model development and validation. A complete report is given in Ref. 11. The analysis concerning the model behavior near outer edges of turbulent regions is briefly explained in Sec. III. The model calibration is described in Sec. IV, and the resulting model is summarized in the Appendix. Owing to space limitations, only two examples of validation computations are given in Sec. V. These are the separating adverse-pressure-gradient boundary layer experimentally studied by Driver¹⁶ and flow past a three-element high-lift airfoil National High Lift Program two dimensional (NHLP 2D)¹⁷ at 20-deg incidence. More validation results are given in Ref. 11.

II. Starting Point

The scale-determining part of the new k - ω model as well as Menter's model and other k - ω models of its form can be written as

$$\frac{Dk}{Dt} = P - \beta^* k \omega + \frac{\partial}{\partial x_k} \left[(v + \sigma_k v_T) \frac{\partial k}{\partial x_k} \right] \quad (1)$$

$$\frac{D\omega}{Dt} = \gamma \frac{\omega}{k} P - \beta \omega^2 + \frac{\partial}{\partial x_k} \left[(v + \sigma_\omega v_T) \frac{\partial \omega}{\partial x_k} \right] + \sigma_d \frac{1}{\omega} \frac{\partial k}{\partial x_k} \frac{\partial \omega}{\partial x_k} \quad (2)$$

with

$$P = -\overline{u'_i u'_i} \frac{\partial U_k}{\partial x_i}, \quad v_T = \frac{C_\mu}{\beta^*} \frac{k}{\omega} \quad (3)$$

where the Reynolds-stress tensor $\overline{u'_i u'_j}$ and C_μ are provided by the constitutive model. The EARSM developed by Wallin and Johansson³ is chosen as the constitutive model in this study. The new model as well as Menter's models employ two sets of model coefficient values that are mixed as

$$C = f_{\text{mix}} C_1 + (1 - f_{\text{mix}}) C_2 \quad (4)$$

where C represents any of the model coefficients γ , β , σ_k , σ_ω , and σ_d , and f_{mix} is the mixing function. Menter's baseline (BSL) and shear-stress transport (SST) models and a combination of the BSL model and the EARSM are used as reference models in the calibration and validation of the new model.

III. Model Behavior near Edges of Shear Layers

Cazalbou et al.⁸ proposed that behavior of turbulence models near outer edges of shear layers can be understood by studying a simplified problem involving only ordinary differential equations. For the family of k - ω models of the form of Eqs. (1) and (2), these equations are

$$\begin{aligned} \mathcal{V} \frac{dU}{dy} &= \frac{d}{dy} \left(v_T \frac{dU}{dy} \right), & \mathcal{V} \frac{dk}{dy} &= \frac{d}{dy} \left(\sigma_k v_T \frac{dk}{dy} \right) \\ \mathcal{V} \frac{d\omega}{dy} &= \frac{d}{dy} \left(\sigma_\omega v_T \frac{d\omega}{dy} \right) + \sigma_d \frac{v_T}{k} \frac{dk}{dy} \frac{d\omega}{dy} \end{aligned} \quad (5)$$

Note that the source and sink terms have been omitted as negligibly small in the edge region. The convective velocity \mathcal{V} must be assumed constant around the edge. The Reynolds number is assumed high, so that viscosity can be omitted. In this problem, all of the variables U , k , and ω are defined as positive quantities that go to zero on the edge. Thus U can be considered either as a velocity defect of a wakelike flow or a velocity excess of a jet-like flow. Note that Cazalbou et al.⁸ and Kok¹⁰ formulated the problem in a moving coordinate frame to make \mathcal{V} zero. In such a frame, the problem takes the form of an unsteady nonlinear diffusion problem.

This problem can have a solution of a power form

$$U(y) = U_0 f^{\sigma_k \sigma_\omega / (\sigma_\omega - \sigma_k + \sigma_d)} \quad (6)$$

$$k(y) = k_0 f^{\sigma_\omega / (\sigma_\omega - \sigma_k + \sigma_d)} \quad (7)$$

$$\omega(y) = \omega_0 f^{(\sigma_k - \sigma_d) / (\sigma_\omega - \sigma_k + \sigma_d)} \quad (8)$$

where

$$f(y) = \max[(\delta_0 - y)/\delta_0; 0] \quad (9)$$

and U_0 , k_0 , ω_0 , and δ_0 are the characteristic scales of the problem. Cazalbou et al.⁸ as well as Catris and Aupoix⁹ and Kok¹⁰ assumed constant C_μ in the eddy-viscosity formula (3). The power solution is possible provided that $v_T \sim f$. Cazalbou et al.⁸ presented the necessary conditions for such solution to exist.

The power functions (6–8) are not necessarily differentiable on the edge point ($y = \delta_0$) with all values of the model coefficients. Cazalbou et al.⁸ showed that there is a corresponding weak solution in such cases. Note that all existing models do not obey this power solution as the exponents can become negative or unbounded in some cases.

The validity of the preceding analysis to models utilizing nonlinear constitutive relations, such as EARSMS, is not obvious. This is because constant C_μ was assumed. Fortunately, the contribution of the higher-order terms of the constitutive model is negligible near the outer edges of shear layers. Thus, the only difference that actually must be considered is the fact that C_μ is variable in nonlinear constitutive modeling.

The behavior of C_μ as a function of the nondimensional shear rate S must be studied in order to understand the edge behavior of nonlinear models. In general flows, S is defined as $\sqrt{(2S_{ij}S_{ji})}$. In this simplified problem, S is reduced to $\tau dU/dy$. $C_\mu(S)$ in two examples of constitutive models, Wallin and Johansson's EARSMS³ and Menter's SST,² are plotted in Fig. 1. At small values of S , C_μ varies slowly with the EARSMS and has a finite limit close to 0.09 as $S \rightarrow 0$. With the SST, it is constant 0.09 at small values of S . At larger values, say $S > 3$, C_μ decreases approximately inversely proportional to S . In fact, the SST model gives exactly $C_\mu \sim 1/S$ at large shear rates. Now, if $S \rightarrow 0$ toward the edge, we can assume almost constant C_μ in the edge region and the preceding analysis is at least approximately valid.

What happens if S does not go to zero at the edge? This can be studied by extending the analysis to a particular case with $C_\mu \sim f^m$ and $m < 1$. In this case, the solution becomes

$$U(y) = U_0 f^{\sigma_k \sigma_\omega (1-m) / (\sigma_\omega - \sigma_k + \sigma_d)} = U_0 f^{n_u}$$

$$k(y) = k_0 f^{\sigma_\omega (1-m) / (\sigma_\omega - \sigma_k + \sigma_d)} = k_0 f^{n_k}$$

$$\omega(y) = \omega_0 f^{(\sigma_k - \sigma_d)(1-m) / (\sigma_\omega - \sigma_k + \sigma_d)} = \omega_0 f^{n_\omega} \quad (10)$$

It is immediately seen that if C_μ decreases toward the edge as with $m > 0$ the edges in the solutions become sharper. This can well lead to a situation where the velocity exponent n_u , originally larger than one with constant C_μ (i.e., $m = 0$), now becomes less than one. The edge will be perfectly sharp with dU/dy being indefinite always when $n_u \leq 1$ (a weak solution). This is an unphysical situation and

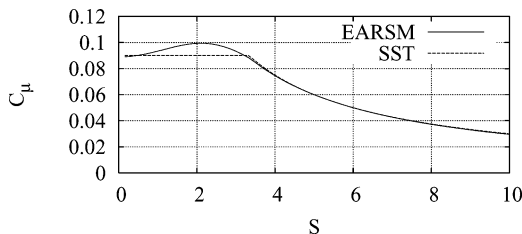


Fig. 1 C_μ as a function of S according to Wallin–Johansson EARSMS³ and Menter's SST model² in simple parallel flows.

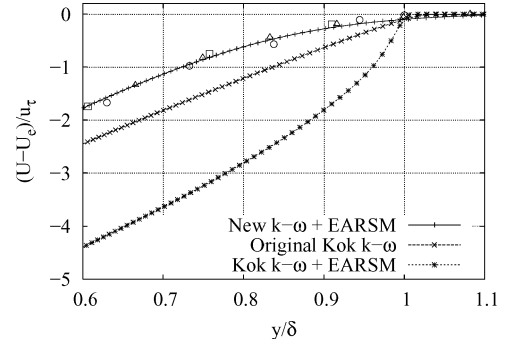


Fig. 2 Numerical solutions of the velocity defect near the outer edge of a self-similar equilibrium boundary layer by using three different k – ω models. Also plotted are experimental data by \circ , Klebanoff¹⁹; \square , Wiegardt and Tillman²⁰; and \triangle , Winter and Gaudet.²¹

can also cause numerical troubles. In practice, the numerical dissipation and the molecular viscosity can alleviate the situation to some extent, but also the numerical solutions will be qualitatively wrong at least when $n_u < 1$.

A situation where S goes to zero as the edge is approached would be favorable. This is achieved when ω decreases more slowly than dU/dy . It is shown in Refs. 11 and 12 that this is ensured by requiring $\sigma_k > 1$. Cazalbou et al.⁸ derived a less restrictive constraint $\sigma_k > 0.5$. This was only to ensure that the source and sink terms of the k equation are negligibly small compared with the transport terms. The new constraint has also physical grounds as $S \rightarrow 0$ at the edge in reality. This new constraint and its physical background is discussed more in detail by Hellsten and Bézard.¹² We must also require that the exponents are positive to ensure that the analysis is valid.^{8–10} This gives us two more constraints. Altogether three constraints are obtained:

$$\sigma_\omega - \sigma_k + \sigma_d > 0 \quad (11)$$

$$\sigma_k - \sigma_d > 0 \quad (12)$$

$$\sigma_k > 1 \quad (13)$$

Most of the existing k – ω models do not satisfy Eq. (13) (Ref. 11). Unphysical sensitivity to the freestream values typical to some k – ω models¹⁸ is also avoided by obeying these constraints. Such sensitivity appears if $\sigma_k = \sigma_\omega$ and $\sigma_d = 0$ (Ref. 11).

Figure 2 shows three different numerical k – ω solutions near the free-stream edge of a self-similar boundary layer. Experimental data by Klebanoff,¹⁹ by Wiegardt and Tillman²⁰ and by Winter and Gaudet²¹ are also plotted. The new model, of which development this paper reports, obeys the preceding constraints and gives a qualitatively correct smooth solution at the edge. Kok's model¹⁰ predicts a sharp edge, and the third case is a generic combination of Kok's model and the EARSMS, which predicts a sharp hook-shaped velocity profile at the edge. Kok's model is designed to satisfy the constraints (11) and (12), but not the constraint (13) as it is a linear Boussinesq model. More specifically, it features $\sigma_k = \frac{2}{3}$, and $\sigma_\omega = \sigma_d = \frac{1}{2}$. The qualities of these numerical solutions are as expected based on the analytical results.

The numerical solutions shown in Fig. 2 are obtained by solving the self-similar equilibrium outer boundary-layer equations (for example, see Wilcox,¹⁵ pp. 155–168). The results have been verified by computing also full Navier–Stokes solutions, which feature the same phenomena.

IV. Calibration

A. Calibration Strategy

Calibration of the model coefficients and the mixing function is described step by step in this section. The final form of the model resulting from these development steps is summarized in the Appendix. The calibration is performed using zero-pressure-gradient (ZPG) and adverse-pressure-gradient (APG) boundary

layers, fully developed plane channel flows, plane far wakes, and mixing layers. The classical constraints for the model coefficients based on the decay of isotropic turbulence in undistorted mean flow, on the homogeneous shear flow, and on the log layer are also exploited.

Before proceeding with the boundary-layer problem, the outer coefficients must be calibrated so that the selected elementary free shear flows, the far wake, and the mixing layer will be predicted with sufficient accuracy. These coefficients also become active on the outer edges of the boundary layers; hence, they must be calibrated before attempting to optimize the inner coefficients for the boundary layer. As already mentioned, Menter's models predict unphysically sharp edges for the turbulent regions. These models also predict wakes and mixing layers to spread far too slowly. To improve the edge behavior, the calibration process must be started from the outer coefficients (set 2).

First, σ_{d2} must be given a much smaller value than $\sigma_{d2} = 2\sigma_{\omega 2} = 1.712$ used in Menter's models to satisfy the constraint (12). Unfortunately, lowering σ_{d2} , without changing any other coefficients, makes the boundary layers spread too rapidly. A value as low as 0.4 is needed to predict the far-wake flow properly. With this value, the boundary-layer thickness would become seriously overpredicted. One way to overcome this contradiction is to change the mixing function in such a way that the change of the model coefficients from the inner (set 1) to the outer (set 2) values takes place farther away from the wall than in Menter's models. It is probably the best practice to design the mixing function in such a way that the change of the coefficients occurs closer to the boundary-layer edge than in Menter's models and to calibrate both coefficient sets to obey the constraints (11–13). Added robustness is achieved by requiring also the inner coefficients to produce acceptably good edge behavior. Choosing this approach means that a value of about 0.4 should be assigned to σ_{d2} , and σ_{d1} should be about 1.0 according to preliminary numerical tests. The outer coefficients will be first looked for, and the modifications to the mixing function will be considered after that in Sec. IV.C.

B. Free Shear Layers

It was already anticipated that σ_{k2} and σ_{d2} should be about 1.1 and 0.4, respectively. On the other hand, γ_2 and β_2 should be calibrated so that ω remains relatively small to allow rapid spreading of free turbulent layers. Numerical experiments showed that the values used in Menter's models $\gamma_2 = 0.44$ and $\beta_2 = 0.0828$ are suitable. These values correspond to the most commonly used k - ε values $C_{\varepsilon 1} = 1.44$ and $C_{\varepsilon 1} = 1.92$. Further numerical tests suggest that 1.0 is a suitable value for $\sigma_{\omega 2}$. Altogether these coefficient values are

$$\begin{aligned}\sigma_{k2} &= 1.1, & \sigma_{\omega 2} &= 1.0, & \sigma_{d2} &= 0.4 \\ \gamma_2 &= 0.44, & \beta_2 &= 0.0828\end{aligned}$$

Mean-velocity profiles of the approximately self-similar far-wake flow are shown in Fig. 3 as functions of the similarity coordinate

$$\eta = (y/D)\sqrt{2D/c_d(x-x_0)} \quad (14)$$

where D is the diameter of the wake-generating cylinder, x is the distance between the cylinder and the measurement station, and x_0 is the location of a virtual origin of the self-similar system. The computed results are numerical solutions of the approximate self-similar equations given for example by Wilcox (Ref. 15, pp. 131–136).

The results computed with the new coefficients are compared with the BSL-EARSM results and with experimental data. The new outer coefficients provide a velocity profile that fares well through the somewhat scattered measurement data. Five sets of measured mean-velocity data are shown: Townsend,²² Thomas,²³ Fabris,²⁴ Antonia and Browne,²⁵ and Weygandt and Mehta.²⁶ Owing to the limited space, the Reynolds-stress distributions are not shown here. These are shown and discussed in detail in Ref. 11.

Figure 4 compares the computed velocity profiles of the self-similar planar mixing layer with experimental data. Again, see

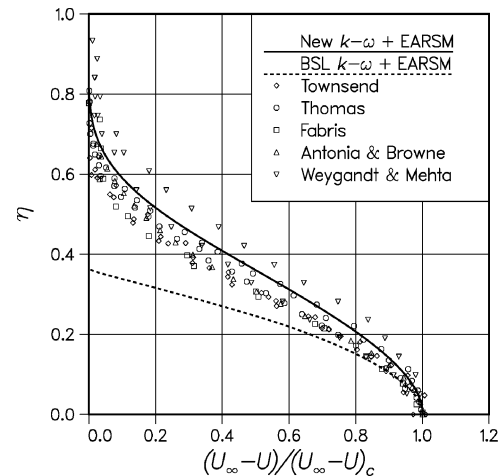


Fig. 3 Velocity profiles of the planar far wake according to the k - ω EARSM model with the new outer coefficients compared with the BSL k - ω EARSM model and experimental data.

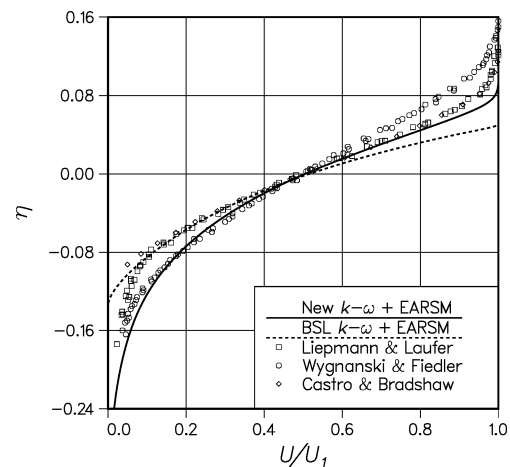


Fig. 4 Velocity profiles of plane mixing layer according to the k - ω EARSM model with the new outer coefficients compared with the BSL k - ω EARSM model and experimental data.

Wilcox (Ref. 15, pp. 131–136) for the self-similar equations. This particular mixing layer is a shear layer between a still fluid and a uniform stream of velocity U_1 . The similarity coordinate is simply $\eta = y/(x - x_0)$. Measurements are by Liepmann and Laufer,²⁷ by Castro and Bradshaw,²⁸ and by Wygnanski and Fiedler.²⁹ The velocity profile measured by Wygnanski and Fiedler shows a clearly higher spreading rate than the other two profiles. The reason for this is not completely clear. This means that the experimental reference data are not as reliable as desired. This has been pointed out by other authors as well.^{30,31} Nevertheless, the new calibration yielded a velocity profile that agrees clearly better with all experiments than the BSL-EARSM on the high-speed side, although it still is somewhat too sharp edged there. However, on the low-speed side the new model agrees better with the data by Wygnanski and Fiedler, whereas the BSL-EARSM results are supported by the other measurements there. Both models give significantly too asymmetric results. Prediction of excessively asymmetric turbulence field in this flow seems to be a common shortcoming of the majority of turbulence models. Transport by the asymmetric mean-velocity field drives the turbulent energy distribution toward asymmetry. However, there must be some counteracting mechanism in the dynamics of turbulent stress evolution because the measurements indicate only very slight asymmetry. This unknown balancing mechanism is not adequately modeled by these models because they provide excessively asymmetric results. This fault seems to be common to most turbulence models as it was detected already in the early days of

Table 1 Spreading rates of different free shear flows

Model	Wake	Mixing layer	Plane jet	Round jet
New $k-\omega$ + EARSIM	0.343	0.104	0.144	0.253
BSL $k-\omega$ + EARSIM	0.237	0.075	0.102	0.130
BSL $k-\omega$	0.239	0.088	0.104	0.120
Experiment	0.3–0.4	0.11	0.10–0.11	0.86–0.96

Reynolds-stress modeling.^{30,31} Attempts were made to find such a calibration that would give less asymmetric results without spoiling the wake-flow results. However, no such values were found.

Also plane and round jets were computed, although this model is not really designed for jet flows. The velocity profiles are not shown here, but the spreading rates are summarized in Table 1 together with the wake and mixing-layer values. The experimental values for the jets are taken from Wilcox.¹⁵ The given mixing-layer value 0.11 matches to the measurements by Liepmann and Laufer²⁷ and by Castro and Bradshaw.²⁸ Wygnanski and Fiedler²⁹ measured a clearly higher spreading rate close to 0.16. The jet spreading-rate values clearly show that the present model is not suitable for jet flows as such as it predicts too rapid spreading of both plane and round jets. Predicting jet flows more accurately requires somewhat increased σ_{d2} and decreased $C_{\omega 2}$, but this might compromise the accuracy in the flows of primary interest in this study.

C. Mixing Function

As proposed in Sec. IV.A, Menter's mixing function F_1 is modified to push the mixing toward the boundary-layer edge. This can be achieved by using the same kind of parameters Γ_1 , Γ_2 , and Γ_3 as used in Menter's models. Only some coefficients have to be changed. Most importantly, Γ_3 has to be multiplied by a factor of, say, 10 to allow the hyperbolic tangent function to remain at unity almost up to the edge. Now, Γ_3 reads

$$\Gamma_3 = \frac{20k}{\max[(\nabla k \cdot \nabla \omega)d^2/\omega; 200k_\infty]} \quad (15)$$

where d is the distance to the nearest wall point. The lower limit of the denominator is made proportional to the far-field value k_∞ . In fully turbulent internal flows, this limiter is of no significance, and any small value can be used. The other parameters Γ_1 and Γ_2 are adopted from the BSL model as such (see the Appendix). However, the final value

$$\Gamma = \min[\max(\Gamma_1; \Gamma_2); \Gamma_3] \quad (16)$$

is multiplied by a factor of 1.5 to obtain the desired behavior. Hence, the final form of the mixing function is given by

$$f_{\text{mix}} = \tanh(1.5\Gamma^4) \quad (17)$$

D. ZPG Boundary Layer

Given a mixing function with the desired behavior, we now look for suitable values for the inner coefficients that give accurate prediction for the ZPG boundary layer and fulfill the edge constraints (11–13). First, it must be remembered that the cross term must not be included in the near-wall region. Therefore, $\nabla k \cdot \nabla \omega$ must be replaced by $\max(\nabla k \cdot \nabla \omega; 0)$ in that term. The diffusion coefficient σ_{k1} must again satisfy the constraint (13). Numerical tests suggest a value of 1.1, which is equal to σ_{k2} . It was also observed that this change removed the anomaly of physically incorrect shape of the velocity profile in the defect layer predicted by the combination of the BSL $k-\omega$ and the EARSIM (Fig. 5). At this point, it was checked that the $k-\omega$ model's ability to fairly accurately model the APG boundary layers is still maintained with the elevated value of σ_{k1} .

The other diffusion coefficient σ_ω has to be kept close to 0.5 in order to maintain the favorable feature of the $k-\omega$ models that they can be solved down to the wall without any near-wall modifications. Extensive numerical experimenting with the ZPG boundary layer

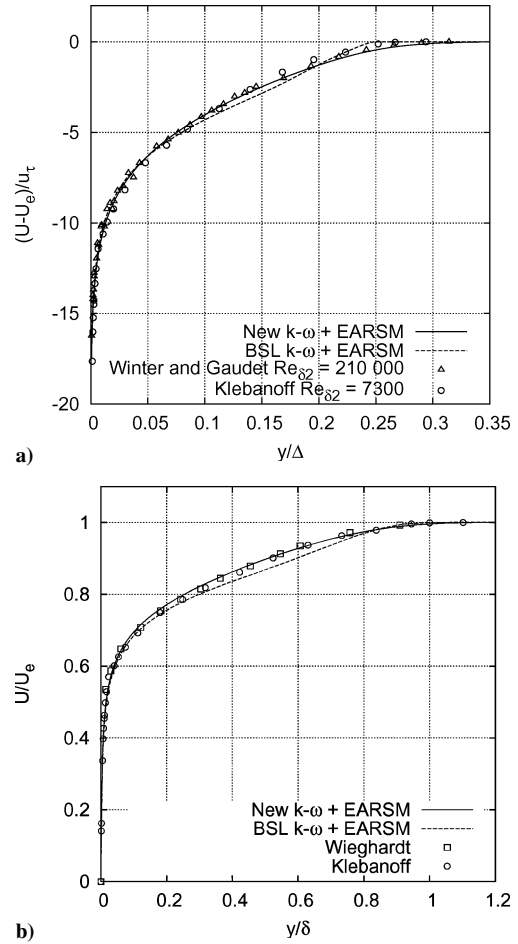


Fig. 5 Velocity-defect profiles through a ZPG boundary layer according to the new $k-\omega$ EARSIM model and with the BSL $k-\omega$ EARSIM: a) self-similar outer-layer computations with experimental data at Δ , high Reynolds number²¹ and \circ , modest Reynolds number¹⁹ and b) full Navier-Stokes computations at modest $Re_{\delta_2} \approx 7.3 \times 10^3$ ($Re_x = 4.2 \times 10^6$) with experimental data by \circ , Klebanoff¹⁹ and \square , Wiegardt and Tillman.²⁰

and with the fully developed channel flow showed that the following values are close to optimum:

$$\begin{aligned} \sigma_{k1} &= 1.1, & \sigma_{\omega 1} &= 0.53, & \sigma_{d1} &= 1.0 \\ \gamma_1 &= 0.518, & \beta_1 &= 0.0747 \end{aligned}$$

Note that γ_1 , β_1 , and $\sigma_{\omega 1}$ are related through the log-layer relation

$$\gamma_1 = \beta_1 / \beta^* - \kappa^2 \sigma_{\omega 1} / \sqrt{\beta^*} \quad (18)$$

with $\beta^* = 0.09$ and $\kappa = 0.42$. Note that Menter's models use $\kappa = 0.41$ here. The selected inner diffusion coefficients satisfy the constraints (11–13) as well as the outer values.

Most of the numerous boundary-layer computations needed in the calibration process were made by numerically solving the approximate self-similar outer-layer equations at the limit $Re \rightarrow \infty$ using the log-law boundary conditions (see Wilcox,¹⁵ pp. 155–168). The similarity variable is $(U_e - U)/u_\tau = f(y/\Delta)$. The self-similar ZPG boundary-layer results were verified by full Navier-Stokes computations using the FINFLO solver.^{32,33} The velocity profiles are shown in Fig. 5 and the turbulent shear-stress distribution in Fig. 6. The new model gives clearly a smoother edge for the boundary layer and velocity profile with a correct shape in the outer layer.

The self-similar velocity profiles are compared with experimental data by Klebanoff¹⁹ ($Re_{\delta_2} \approx 7.3 \times 10^3$) and by Winter and Gaudet²¹ ($Re_{\delta_2} \approx 2.1 \times 10^5$). The result computed using the new model agrees better with the high-Reynolds-number data. This is reasonable because $Re \rightarrow \infty$ was assumed in the derivation of the self-similar equations.

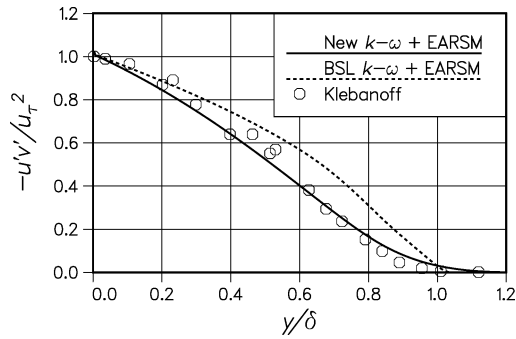
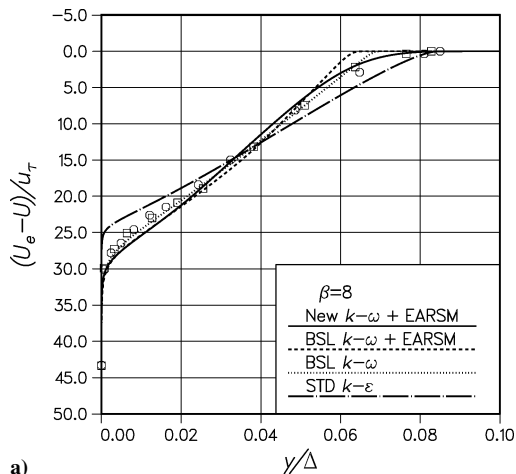
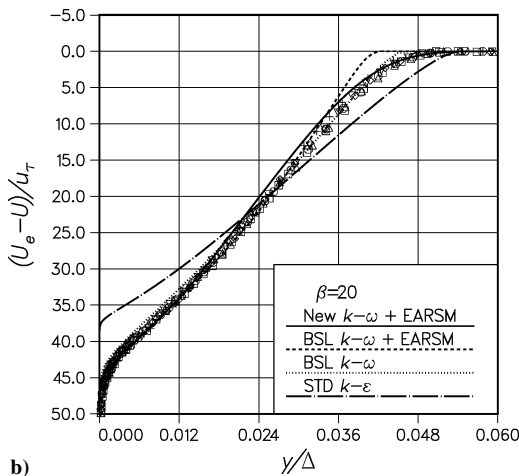


Fig. 6 Shear-stress profiles through a ZPG boundary layer according to the new $k-\omega$ EARSIM model and with the BSL $k-\omega$ EARSIM. Computed results are numerical solutions of the self-similar equations: \circ , experimental data by Klebanoff.¹⁹



a)



b)

Fig. 7 Velocity-defect profiles of two equilibrium boundary layers with different pressure gradients. Different symbols are used to separate measurements at different locations in the same experiment.

E. Equilibrium APG Boundary Layers

So far, boundary-layer results have been shown only for the ZPG case. Next, the performance of the proposed model is investigated in equilibrium boundary layers with different nonzero pressure gradients. The nondimensional pressure-gradient parameter β_T is constant in equilibrium boundary layers. Computed results are again based on the self-similar outer-layer equations (see Wilcox,¹⁵ pp. 155–168).

Reference 11 reports the computed mean-velocity profiles of six cases with β_T ranging from -0.35 to about 20 together with experimental data. It also involves a more detailed study of the strongest adverse-pressure-gradient case ($\beta_T = 20$). Only two cases are shown here because of the limited space (Fig. 7). The first case has $\beta_T \approx 8$,

and Clauser's experimental data,³⁴ taken from Ref. 35, is used as a reference. The second case features even stronger pressure gradient $\beta_T \approx 20$. The experimental data are from Skårre and Krogstad.³⁶ The $k-\omega$ results are compared also with the results computed using the standard $k-\epsilon$ model.³⁷

The predicted velocity profiles involving $k-\omega$ modeling agree fairly well with the measured data. The role of the constitutive model is not as important here as in the nonequilibrium situations usually occurring in practical flow problems. Therefore, the original linear BSL model is no worse in this case than the BSL-EARSIM version. The velocity profiles computed using the new model and the BSL-EARSIM are relatively similar to each other except near the outer edges. As expected, the velocity profiles computed employing the new model are in clearly better agreement with the measurement data on the edge regions. The differences between the results would increase in favor of the new model if the y coordinate were scaled by the boundary-layer thickness δ instead of Δ .

In contrast to all of the $k-\omega$ results, the standard $k-\epsilon$ model is in strong disagreement with the experimental data. It gives too low a velocity defect near the wall. The velocity profiles are not only excessively full, but the overpredicted friction velocity u_τ further increases the error. This is typically seen as overestimated skin friction and delayed separation in practical flow simulations. This shortcoming of the $k-\epsilon$ models has been known for quite a long time.^{2,14,38}

The $k-\epsilon$ model used for the preceding comparisons is a standard linear Boussinesq model. The use of higher-order constitutive models, like SST or EARSIM, does not resolve the overestimation of the wall-layer length scale. Higher-order constitutive models typically give some improvements in predicting nonequilibrium flows, but a $k-\epsilon$ model furnished with a higher-order constitutive model will still suffer from overestimated turbulent mixing near the wall. This has been shown in Ref. 6, where separating APG flows were computed using linear $k-\epsilon$ and $k-\omega$ models, SST $k-\omega$, and EARSIM based on the $k-\epsilon$ and $k-\omega$ models. The linear models failed completely, whereas the SST and the EARSIM $k-\omega$ models gave satisfactory results. The $k-\epsilon$ EARSIM model was much better than the linear one, but, very importantly, near the wall it failed almost similarly to the linear $k-\epsilon$ model. In one of the cases, it completely refused to predict separation.

F. Wall-Boundary Conditions

The usual no-slip condition ($k = 0$ on the wall) is given for k on wall boundaries. The wall-boundary condition for ω is not that obvious because theoretically ω has a singularity on a solid wall. As recently suggested by Gullman-Strand et al.,³⁹ ω can be split into two as $\omega = \tilde{\omega} + \omega_w$, where ω_w is the general analytical near-wall solution. Substitution of this into the ω -model equation yields a new form in which $\tilde{\omega}$ is the variable to be solved. The singularity can be avoided this way. Gullman-Strand et al. showed how the present model can be transformed and operated in the $\tilde{\omega}$ form.^{39,40} The development of the present model was partially done before Gullman-Strand's work, and therefore the method developed in Ref. 41 is employed here for ω wall-boundary condition. However, the author wants to encourage the readers to try Gullman-Strand's technique although it is not employed in this work.

The present method is based on Wilcox's rough-wall boundary condition method,^{14,15} in which $\omega_w = u_\tau^2 S_R / \nu$ with S_R being a nondimensional function defined as

$$S_R = \begin{cases} [50 / \max(k_s^+; k_{s\min}^+)]^2 & \text{for } k_s^+ < 25 \\ 100 / k_s^+ & \text{for } k_s^+ \geq 25 \end{cases} \quad (19)$$

and k_s^+ is the inner-scaled sand-roughness height $k_s u_\tau / \nu$, so that rough walls can be simulated if the equivalent sand roughness can be estimated. For smooth walls, $k_{s\min}^+$ becomes active. It is known from experiments that the surface roughness does not influence the flow if k_s^+ is less than, say, 4 . The computed wall shear stress is, however, quite sensitive to the choice of $k_{s\min}^+$ (Refs. 41 and 42). The optimal value is a function of the grid spacing next to the wall. It has been found in Ref. 41 that the grid sensitivity can be largely eliminated if $k_{s\min}^+$ is defined as a function of the inner-scaled thickness of the first

control volume, or more generally as a function of the inner-scaled wall distance of the first node from the wall d_1^+ , as follows:

$$k_{s\min}^+ = \min \left[4.3(d_1^+)^{0.85}; 8 \right] \quad (20)$$

Equation (20) was originally optimized for the $k-\omega$ SST model, but it turned out that it works as well with the new model.

V. Validation

A. General Remarks

The preliminary validation included computations of several two-dimensional flow problems employing the FINFLO code.^{32,33} A developing wake, a separating APG boundary layer, massively separated flow in an asymmetric diffuser, two single-element airfoil flows near maximum lift, and flow past a three-element airfoil in high-lift conditions were computed. As mentioned in the Introduction, only two cases, the separating APG boundary layer and the three-element airfoil case, are presented here owing to the limited space. For the complete report, see Ref. 11. The proposed model showed either better or similar accuracy also in those cases not presented here, except in the diffuser case where the proposed model slightly overestimated the extent of separated flow.

B. Separating Adverse-Pressure-Gradient Boundary Layer

Equilibrium APG boundary layers were studied in Sec. IV.E. Such equilibrium boundary layers can be set up in a laboratory, and the equilibrium is a very beneficial state of affairs in research work. In practical engineering problems, however, the APG boundary layers are extremely seldom in equilibrium. The boundary layers on the upper surfaces of wing elements are typically subjected to pressure gradients that produce increasing β_r values. These kinds of situations often lead to separation. Because the physics involved in the high-lift airfoil problems is quite complex, even in single-element cases, the studies of separating APG boundary layers are started from a simpler, more idealized flow problem. The decelerating boundary-layer flow along a circular cylinder is a suitable case for this purpose (Fig. 8). The measurements have been made by Driver.¹⁶ This flow was one of the cases in Ref. 6 to study the effect of the constitutive and the scale-determining models in separating APG boundary-layer problems.

The cylinder axis is oriented in the streamwise direction, and the test-section walls are diverged in order to decelerate the flow. The inflow Reynolds number based on the cylinder diameter D is 2.8×10^5 and about 4×10^3 based on the inlet momentum thickness δ_2 . The inflow boundary conditions have been obtained from the result of a separate computation of a ZPG boundary layer on the same cylinder. The outer edge is modeled as an inviscid slip wall contoured according to the streamlines plotted by Driver. This slip wall had to be placed quite close to the outer edge of the boundary layer because no streamline information was available further away. The influence of this fact could not be studied, unfortunately. The computational grid consisted of 160×96 control volumes in the axial and radial directions, respectively. The grid independence was studied in Ref. 6 by repeating one computation employing Menter's model using a 320×192 grid (not shown here). Virtually unchanged results were obtained, except that the edge of the boundary layer became slightly sharper as the grid was refined. The new model does not share this particular grid-dependency problem as it predicts smooth outer edges.

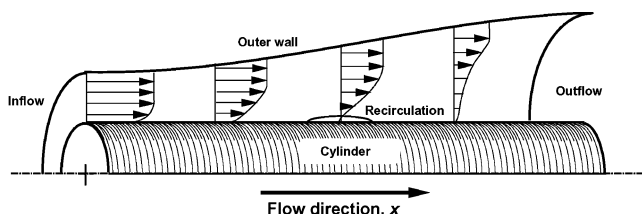


Fig. 8 Schematic illustration of Driver's decelerating boundary layer.

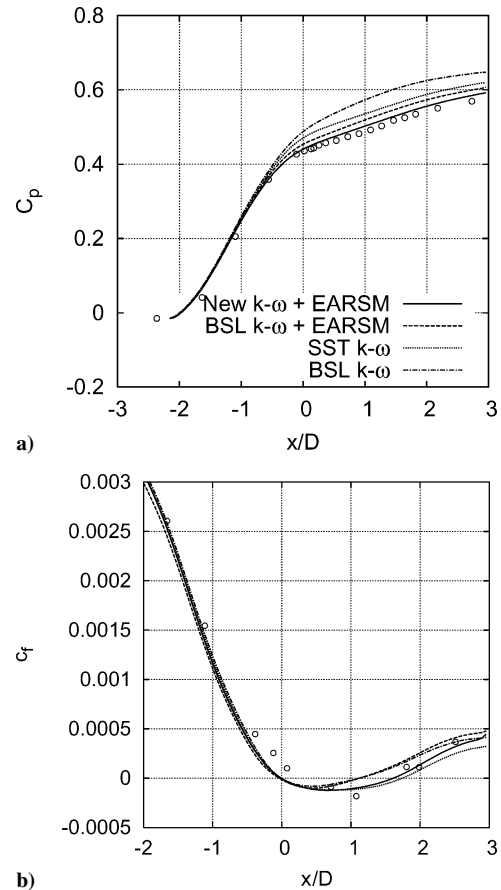


Fig. 9 Coefficients for a) pressure C_p and b) skin-friction coefficient c_f along the cylinder surface in Driver's decelerating boundary layer.

The pressure and skin-friction distributions are plotted in Fig. 9. One can immediately observe that the original BSL model underestimates the pressure loss more significantly than the EARS-based models and the SST model. Hence, it can be assumed that the role of the constitutive model is important in this flow. This has been shown by Menter in the case of the SST-model² and later by Hellsten using also EARS-based models.⁶ All of the $k-\omega$ models predict the flow separation at almost the same location, which is only slightly upstream from the measured separation line. The new model and the SST model predict slightly longer separation bubbles than the BSL models. On the other hand, the pressure distribution predicted with the new model is closer to the measurements than that of the SST and BSL-EARS. SST predicts a slightly lower loss than the EARS-based models. The original SST results presented by Menter² showed slightly higher pressure loss. This difference might be explained by different grid resolutions. It was shown in Ref. 6 that the $k-\varepsilon$ models do not predict separation at all, regardless of the employed constitutive model, Boussinesq, or EARS. Nevertheless, the EARS-based $k-\varepsilon$ predicted a significantly larger pressure loss than the linear Boussinesq $k-\varepsilon$ model. This is yet further evidence that the most significant difference between the $k-\varepsilon$ and $k-\omega$ models in APG flows takes place near the wall.

The velocity and Reynolds shear-stress profiles around the separation bubble are plotted in Fig. 10 at five stations: $x/D = -0.091, 0.363, 1.088, 1.633$, and 2.177 . The velocity profiles show that the BSL model underestimates the extent of separation. The reversed flow is restricted into an extremely thin region near the wall. The BSL-EARS also underestimates the extent of separation, and it predicts the flow to reattach and to recover somewhat too early. This was observed already in Ref. 6. The new model is seen to perform somewhat better in this regard, although it still slightly underpredicts the backflow and the flow retardation over the bubble. The accuracy of the new model in this particular case is quite similar to that of the SST model. The shear-stress curves in Fig. 10 just show

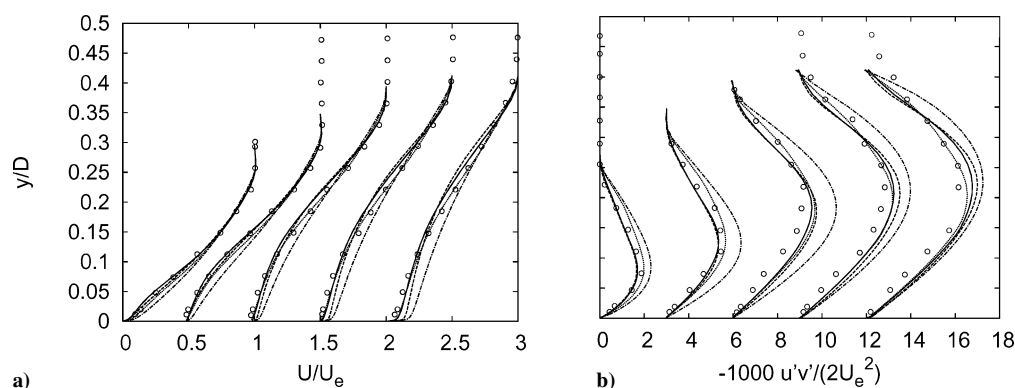


Fig. 10 Profiles of a) velocity U/U_e and b) Reynolds shear-stress $-\overline{u'v'}/(2U_e^2)$ profiles in Driver's decelerating axisymmetric boundary layer at five stations: $x/D = -0.091, 0.363, 1.088, 1.633$, and 2.177 . Note the shifted origin of each station. Legends as in Fig. 9.

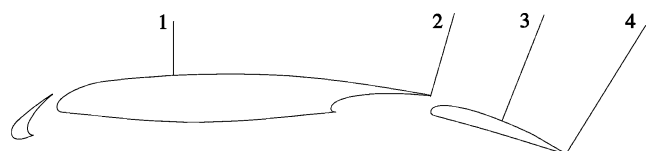


Fig. 11 Geometry of the NHLP 2D airfoil with lines indicating the stations where total-pressure distributions are measured.

how the linear BSL model overestimates the shear stress indicating the importance of the advanced constitutive modeling in these kinds of flows. The reduced shear stress predicted with the SST and the EARSM-based models is primarily owing to a reduction of the shear-stress anisotropy $a_{12} = \overline{u'v'}/k$ instead of a reduction of k .

C. High-Lift Airfoil Flows

Reference 11 reports three airfoil computations, each of them at only one angle of attack. This should be considered only as a preliminary validation and a feasibility study of the new model. More comprehensive validation is beyond the scope of this study. Owing to the space limitations, only one of these three computations is presented here, whereas the other two are only briefly discussed next.

The three cases were selected to reflect somewhat different flows past two-dimensional airfoil sections near maximum lift. The first case is the single-element Aerospatiale A airfoil at an angle of attack of 13.3° (Ref. 43). In this case, the flow on the upper surface separates near the trailing edge. The recirculation region is small, and the separation can be classified as mild. The results computed with the new model are in good agreement with the experiments.¹¹

The second case is also a single-element airfoil NACA-4412 at 13.87° . This situation differs from the first one in the extent of separation. Now, there is a substantial region of backflow with a rather strong displacement effect. This is computationally a very hard case, because the models tended to predict time-dependent results as the grid was refined. Unfortunately, proper grid convergence was not achieved in this case.¹¹ Again, the new model gave results in good agreement with the measurements by Coles and Wadcock.⁴⁴ However, reliable conclusions cannot be made in this case owing to the lack of adequate grid convergence.

Most of the real-life high-lift aerodynamics deals with multielement wing sections. Therefore, the NHLP 2D three-element airfoil at 20.18° was selected as the final case (Fig. 11). This case is discussed below in more detail and some results are presented.

Flows about multielement airfoils involve added complexity in comparison with the single-element problems. Not only are the geometry and the grid generation more complex in multielement cases, but they also involve more complex flow details. The confluent and possibly merging boundary layers, wakes, and mixing layers become important. The main goal in this study was to develop a turbulence model that is more suitable for these kinds of problems than the existing models. Therefore, such a flow problem is selected as the final test case, although the focus of this study is in the basic development.

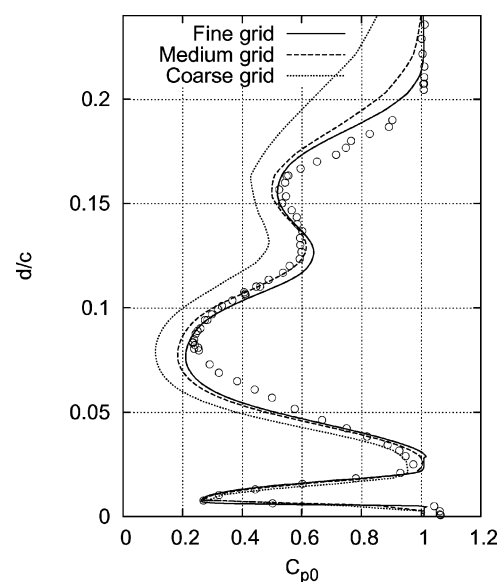


Fig. 12 Grid-convergence study using the new $k-\omega$ EARSM model. Distributions of the total-pressure coefficient through the confluent wakes at just behind the flap trailing edge.

As this is a takeoff configuration with the slat angle of 25° and flap angle of only 20° , there is no substantial flow separation, and this makes it somewhat easier for the turbulence model to yield accurate results. The focus is kept on the wake/boundary-layer interaction process, pressure distributions, and on the integrated lift and drag coefficients. The model's ability to predict the separation of boundary layers without wake interaction has already been assessed in Sec. V.B, and in Ref. 11 for the single-element airfoil cases. The angle of attack is 20.18° in this case, and the chord Reynolds number and the freestream Mach number are 3.52×10^6 and 0.197 , respectively.

The measurements were performed in the early 1970s by the former British Aerospace Company. The results are reported by Moir.¹⁷ The experimental results include the lift and drag coefficients, pressure distributions along the surfaces of each element, and total-pressure coefficient distributions through the boundary layer and confluent wakes at four stations on the main wing and flap upper surfaces (Fig. 11). This flow case has been previously studied computationally by several groups as summarized by Fejtek.⁴⁵ To mention only a few earlier works, Rumsey et al.⁴⁶ has studied this case as well as Rudnik.⁴⁷ Recently Wild studied computational fluid dynamics (CFD)-based airfoil optimization using, for example, this case.⁴⁸ Wild reported transition locations for each element obtained by means of a boundary-layer stability calculations using the e^n method. This information, although its reliability is not fully known, is highly useful for all current and future CFD studies of this case. These transition locations were used in this study.

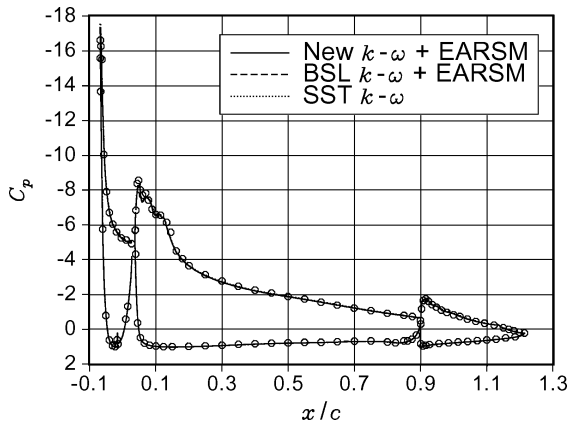


Fig. 13 Computed and measured pressure-coefficient distributions along the NHP 2D airfoil surfaces.

The present computations were made using a relatively fine grid that consists of 364,608 control volumes in 17 blocks. The computational domain extended about 50 chord lengths away from the airfoil, and so-called circulation correction or point-vortex correction was employed in the far-field boundary.¹¹ The grid convergence is studied by comparing the aerodynamic force coefficients computed with the fine grid and with medium and coarse grids (see Table 2). The medium grid was obtained from the fine grid by omitting every second grid line in both directions. The coarse grid, in turn, was obtained similarly from the medium grid. Also, the total-pressure profiles computed using these three grids are compared. These profiles at the rearmost measurement station are shown in Fig. 12. The grid-convergence study was made using the new model only. Both comparisons indicate that the fine-grid results are not fully grid independent but, nevertheless, reasonably grid converged. Only the fine-grid results are used for turbulence model comparisons. All of the fine-grid computations refused to converge to a stationary result using the pseudo time integration.

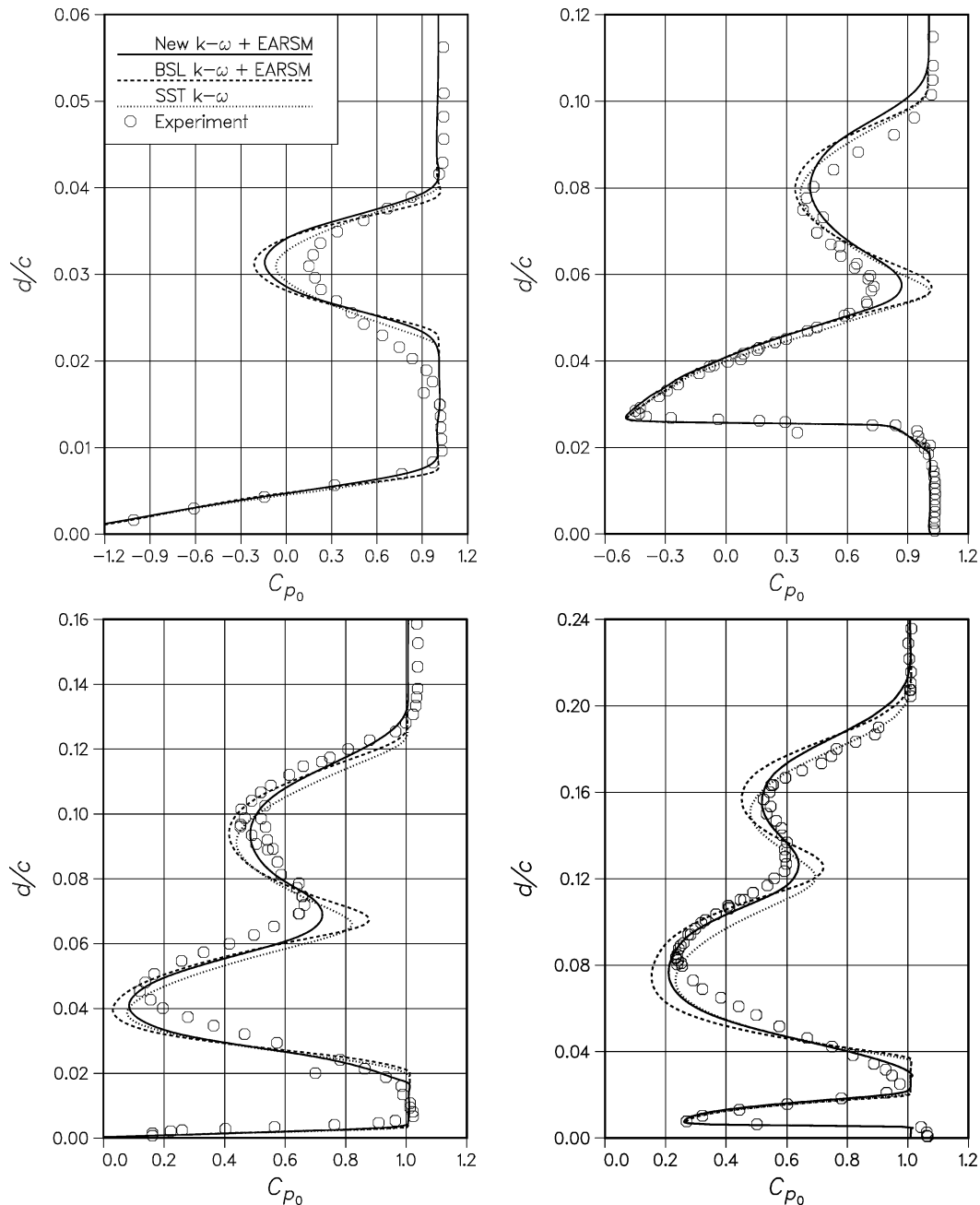


Fig. 14 Distributions of the total-pressure coefficient C_{p0} at locations 1 (upper left) to 4 (lower right) given in Fig. 11.

Table 2 Grid-dependency of the lift and drag coefficients of the NHLP 2D airfoil computed with the new model

Grid	Control volumes	c_l	c_d
Coarse	22,788	3.94	0.083
Medium	91,152	4.03	0.061
Fine	364,608	4.06	0.057

Table 3 Comparison of the lift and drag coefficients of the NHLP 2D airfoil computed with different turbulence models

Model	c_l	c_d
New $k-\omega$ EARSMS	4.06	0.057
BSL $k-\omega$ EARSMS	4.05	0.056
SST $k-\omega$	4.09	0.055
Rumsey ⁴⁶ ($k-\omega$ EARSMS)	4.08	0.068
Rudnik ⁴⁷ (Wilcox's $k-\omega$)	4.01	0.071
Experiment, uncorrected	4.11	0.055
Experiment, corrected	4.11	0.068

Stationary solutions were obtained by means of time-accurate simulations.

The computed and measured lift and drag coefficients are shown in Table 3, which also includes the $k-\omega$ EARSMS results by Rumsey et al. and Rudnik's results. The lift coefficients were predicted within the experimental uncertainty with all three models. In general, the differences in lift coefficients predicted with different models are insignificant in this case. This can also be seen in Fig. 13, which shows the surface-pressure coefficient distributions. The curves are practically indistinguishable. The predicted drag coefficients are quite clearly lower than the experimental wind-tunnel corrected value. Incidentally, the predicted values agree very well with the measured uncorrected drag coefficient. Rudnik's computation provided a slightly lower lift coefficient and a clearly higher drag that agrees with the measurement. It is reasonable to assume that the grid used by Rudnik caused more numerical dissipation than the present grid (see the discussion in Ref. 11). If this is true, it means that an asymptotic numerical result in which the numerical errors approach zero would predict an even lower drag coefficient than the present computations. However, even this does not mean that the models are fully responsible for the underpredicted drag. Uncertain transition locations and the fact that the computations simulate a freestream situation instead of the confined experimental situation are, indeed, significant factors causing differences between the computed and measured drag; predicting the drag of a high-lift configuration is a very difficult task, as pointed out by Fejtek.⁴⁵

The total-pressure coefficient C_{p0} profiles through the upper surface boundary layers of the main wing and the flap and through the confluent wakes are shown in Fig. 14. Menter's SST model² is also included in the comparison. In this case, the interactions between the wakes and boundary layers are weak and do not influence the aerodynamic forces. At a slightly higher angle of attack, the interactions might become more important. The present results give, however, some impression about the ability of the new model to predict the merger of the wakes and boundary layers. The first plot in Fig. 14 is over the main wing at a location of 35% of the stowed chord. Here, the predicted wake is too symmetric in comparison with the experiment, which means that the turbulent shear stress is underestimated on the inner side of the wake. Possibly incorrectly predicted transport of the turbulent stresses generated in the slat cove might be a reason. Such fault could be a consequence of the weak equilibrium assumption in the derivation of the constitutive model and could only be avoided by using an RST model. Unfortunately, all attempts to compute this flow with an RST model failed to converge. It was also speculated in Ref. 11 that the effect of the wake curvature, which is destabilizing on the inner side of the wake, might have been one reason for the underestimation of the turbulent shear stress on the inner side of the wake. Recent computations with the curvature-corrected EARSMS, see Eqs. (A10) and (A11) in the Appendix, suggest, however, that the curvature effects are not likely

to be important here. The influence of the curvature correction was small in this case; hence, the results are not shown here. As the curvature correction deteriorated, the stability and the convergence rate significantly, it seems to not be worth using in this particular case.

At the main-wing trailing edge, the wake is predicted to be slightly further away from the wing surface in comparison with the measurement data. This might be owing to the just-discussed underestimated turbulence on the inner side of the wake. The fact that the new model predicts a more rapidly spreading wake than the BSL-EARSMS or the SST model can be seen at this station. The merger of the wake and the boundary layer has already begun at this station according to the measurements. The new model predicts this better than the BSL-EARSMS and the SST models. This is even more clearly seen at the next stations, that is, at the flap midchord and at the trailing edge of the flap. The plots in the last two stations reveal that also the main-element wake is predicted slightly too symmetric quite similarly as the slat wake. Again, failure in modeling the anisotropy transport from the flap cove might possibly explain this.

In general, the computed results, except for the drag coefficient, are in a better agreement with the measurements than the earlier computations.⁴⁵⁻⁴⁸ However, Rumsey recently repeated his computations using the present grid and transition locations and plotted the C_{p0} distributions along exactly the same lines as here, and his new results were in rather good agreement with the present results (Rumsey, private communication, 2004). The new model seems to predict the evolution of the wakes and the merger processes quite accurately, except that the slat wake asymmetry is not correctly predicted.

VI. Conclusions

A new two-equation turbulence model was developed for computational aerodynamics purposes, especially for high-lift aerodynamics applications. The new model employs the explicit algebraic Reynolds-stress model (EARSMS) developed by Wallin and Johansson³ as the constitutive relation between the turbulent stress tensor and the mean-velocity gradient. The new scale-determining model is based on the $k-\omega$ formulation. The model equations are of similar form to Menter's $k-\omega$ models,² but the model is completely recalibrated. Particular attention was paid to the model's sensitivity to pressure gradients, to the behavior near the outer edges of turbulent flows, and to the calibration of the model coefficients for flow phenomena relevant to high-lift aerodynamics. The model development was based on both analytical studies and numerical experimenting. New values for the model coefficients were found, leading to improvements in comparison with Menter's models and other previously proposed $k-\omega$ models.

The analysis concerning the model behavior near the edges of turbulent regions⁸⁻¹⁰ was extended for models involving variable C_μ coefficient such as EARSMSs. This analysis is a very useful tool providing understanding of anomalies occurring with many $k-\omega$ models near the edges of turbulent flows. The analysis explains these anomalies, and it provides constraints for the diffusion coefficients to avoid such unphysical solutions. These constraints were very useful in the calibration process.

The model calibration was carried out by means of a large number of numerical computations of selected elementary flows. The elementary flow problems were formulated in a self-similar form in order to facilitate quick and grid-independent numerical solution and thus the large number of computations needed in the calibration process. Also, more realistic two-dimensional flows were computed already during the calibration process. The proposed new model is believed to be applicable to a wider range of flows than most of the other $k-\omega$ models. This is owing to two reasons. First, the EARSMS constitutive model has a wider range of applicability than the linear Boussinesq relation, which is used in most of the other $k-\omega$ models. Second, a relatively wide base of different flows was used in the calibration.

Finally, the new model was preliminarily assessed and validated using a set of realistic flow problems, including high-lift airfoil flows. The new model showed relatively good behavior in the considered test cases. Improvements over the reference models were

achieved especially near the edges of turbulent regions and also in predicting flows with mild separation. A three-element airfoil at a high angle of attack was studied as the final validation case. The new model predicted the evolution of the wakes and the merger process of the wakes and boundary layers somewhat more accurately than the reference models. However, the new model as well as the reference models predicted a too symmetric slat wake.

The proposed new k - ω EARS model is a promising model to be employed in practical computational-fluid-dynamics (CFD) work in aerodynamic design and analysis. It is relatively easy to implement, particularly in the CFD packages already equipped with Menter's k - ω model.

Appendix: Summary of the New Model

Scale-Determining Model

The transport equations for k and ω of the new k - ω model are written as

$$\frac{Dk}{Dt} = P - \beta^* k \omega + \frac{\partial}{\partial x_k} \left[(v + \sigma_k v_T) \frac{\partial k}{\partial x_k} \right] \quad (A1)$$

$$\begin{aligned} \frac{D\omega}{Dt} = & \gamma \frac{\omega}{k} P - \beta \omega^2 + \frac{\partial}{\partial x_k} \left[(v + \sigma_\omega v_T) \frac{\partial \omega}{\partial x_k} \right] \\ & + \sigma_d \frac{1}{\omega} \max \left(\frac{\partial k}{\partial x_k} \frac{\partial \omega}{\partial x_k}; 0 \right) \end{aligned} \quad (A2)$$

Note that the cross term in the ω equation is included only when the inner product of the gradients of k and ω is positive. The model coefficients vary in space as $C = f_{\text{mix}} C_1 + (1 - f_{\text{mix}}) C_2$, where C represents any of the model coefficients $\gamma, \beta, \sigma_k, \sigma_\omega$, and σ_d , and f_{mix} is a new mixing function (replacing Menter's F_1) and is described next. $\beta^* = 0.09$ and the other coefficient values of the new model are shown in Table A1.

The mixing function f_{mix} is slightly modified from Menter's corresponding function F_1 but is based on the same ideas. The mixing function is equal to one almost up to the edge of boundary layers and is zero in the free turbulent flows and in laminar regions. Wall distance is needed also in this model. The ratio of turbulent length scale and wall distance d is used as the first measure just as in the BSL model, $\Gamma_1 = \sqrt{k}/(\beta^* \omega d)$. The second measure is based on the viscous length scale and reads $\Gamma_2 = 500\nu/(\omega d^2)$, and maximum of Γ_1 and Γ_2 is taken. Following Menter, even a third measure is exploited. This is based on the length scale of the cross term $(\nabla k \cdot \nabla \omega)/\omega$ and the wall distance, and it is used as an upper bound for the maximum of Γ_1 and Γ_2 . The redefinition for Γ_3 is given by

$$\Gamma_3 = \frac{20k}{\max [d^2 (\nabla k \cdot \nabla \omega)/\omega; 200k_\infty]} \quad (A3)$$

with k_∞ being the user-specified small far-field value of k . In fully turbulent internal flows this limiter is of no significance; thus, any small value can be used. Finally, the mixing function is defined as

$$f_{\text{mix}} = \tanh (1.5 \Gamma^4) \quad (A4)$$

$$\Gamma = \min [\max (\Gamma_1; \Gamma_2); \Gamma_3] \quad (A5)$$

It has been shown in Ref. 11 that the model is reasonably insensitive to the freestream values of k and ω provided that excessively high values are not given. The wall-boundary condition for k is the usual no-slip condition ($k = 0$ on the wall), and the recommended wall value for ω can be computed from $\omega_w = u_\tau^2 S_R/\nu$, where S_R is

defined as

$$S_R = \begin{cases} [50/\max(k_s^+; k_{s\min}^+)]^2 & \text{for } k_s^+ < 25 \\ 100/k_s^+ & \text{for } k_s^+ \geq 25 \end{cases} \quad (A6)$$

with k_s specified for rough walls, and for smooth walls

$$k_{s\min}^+ = \min [4.3(d_1^+)^{0.85}; 8] \quad (A7)$$

with d_1^+ being the inner-scaled wall distance of the first node adjacent to a wall.

Constitutive Model

The proposed k - ω model is designed to be used with the EARS model developed by Wallin and Johansson³ as the constitutive model. The model is written for the Reynolds-stress anisotropy tensor a_{ij} . The formulation of the algebraic Reynolds-stress model is not repeated here; only its explicit solution is given. The anisotropy tensor is expressed using the following tensor polynomial:

$$\begin{aligned} a_{ij} = & \beta_1 S_{ij} + \beta_3 (\Omega_{ik}^* \Omega_{kj}^* - \frac{1}{3} I_\Omega \delta_{ij}) + \beta_4 (S_{ik} \Omega_{kj}^* - \Omega_{ik}^* S_{kj}) \\ & + \beta_6 (S_{ik} \Omega_{kl}^* \Omega_{lj}^* + \Omega_{ik}^* \Omega_{kl}^* S_{lj} - \frac{2}{3} IV \delta_{ij}) + \beta_9 (\Omega_{ik}^* S_{kl} \Omega_{lm}^* \Omega_{mj}^* \\ & - \Omega_{ik}^* \Omega_{kl}^* S_{lm} \Omega_{mj}^*) \end{aligned} \quad (A8)$$

where the effective nondimensional vorticity tensor is defined by

$$\Omega_{ij}^* = \Omega_{ij} - (\tau/A_0) \Omega_{ij}^{(r)} \quad (A9)$$

The second term, which depends on $\Omega_{ij}^{(r)}$, is an optional part that can be beneficial if the streamline-curvature effects on turbulence are considered important. However, the model can be operated without adding this so-called vorticity modification caused by curvature.⁴⁹ In fact, the curvature modification was employed in only one of the computations discussed in this paper. This was one of the NHLP 2D computations. Wallin and Johansson calibrated a value of -0.72 for the coefficient A_0 (Ref. 49). $\Omega_{ij}^{(r)}$ is the vorticity modification caused by streamline curvature, and it is calculated from

$$\Omega_{ij}^{(r)} = -\epsilon_{ijk} B_{km} S_{pr} \frac{DS_{rq}}{Dt} \epsilon_{pqm} \quad (A10)$$

with

$$B_{km} = \frac{II_S^2 \delta_{km} + 12 III_S S_{km} + 6 II_S S_{kl} S_{lm}}{2 II_S^3 - 12 III_S^2} \quad (A11)$$

The reader is advised to consult Refs. 49–51 to understand this method.

The timescale τ is simply the turbulent timescale $\tau = 1/(\beta^* \omega)$. The earlier reports^{11,52} included also a viscous timescale as a lower limit. It was dropped after it was found to delay the transition in some cases and because it is not really necessary in this kind of high-Reynolds-number formulation.

The β coefficients in Eq. (A8) are functions of the invariants $II_S = S_{kl} S_{lk}$, $II_\Omega = \Omega_{kl}^* \Omega_{lk}^*$, $III_S = S_{kl} S_{lm} S_{mk}$, and $IV = S_{kl} \Omega_{lm}^* \Omega_{mk}^*$ as follows:

$$\begin{aligned} \beta_1 = & -N(2N^2 - 7II_\Omega)/Q, & \beta_3 = & -12IV/(NQ) \\ \beta_4 = & -2(N^2 - 2II_\Omega)/Q, & \beta_6 = & -6N/Q \\ \beta_9 = & 6/Q \end{aligned} \quad (A12)$$

where the denominator Q reads

$$Q = \frac{5}{6} (N^2 - 2II_\Omega) (2N^2 - II_\Omega) \quad (A13)$$

Table A1 Model coefficients

Set	γ	β	σ_k	σ_ω	σ_d
1	0.518	0.0747	1.1	0.53	1.0
2	0.44	0.0828	1.1	1.0	0.4

In two-dimensional mean flows, only two independent invariants, II_S and II_Ω , exist, and only the first and third terms remain in Eq. (A8):

$$\beta_1 = -\frac{6}{5} \left[N / (N^2 - 2II_\Omega) \right] \quad (A14)$$

$$\beta_4 = -\frac{6}{5} \left[1 / (N^2 - 2II_\Omega) \right] \quad (A15)$$

The function N is solved from a cubic equation in two-dimensional mean flows. In three-dimensional cases, the corresponding equation is of the sixth order, and no explicit solution can be found for it. Therefore, the solution of the cubic equation is used also for three-dimensional cases. It is given by

$$N = \begin{cases} A'_3/3 + (P_1 + \sqrt{P_2})^{1/3} + \text{sign}(P_1 - \sqrt{P_2})|P_1 - \sqrt{P_2}|^{1/3} & \text{for } P_2 \geq 0 \\ A'_3/3 + 2(P_1^2 - P_2)^{1/6} \times \cos \left[\frac{1}{3} \arccos(P_1 / \sqrt{P_1^2 - P_2}) \right] & \text{for } P_2 < 0 \end{cases} \quad (A16)$$

where

$$P_1 = [A'_3/27 + (9/20)II_S - \frac{2}{3}II_\Omega]A'_3 \quad (A17)$$

$$P_2 = P_1^2 - [A'_3/9 + (9/10)II_S + \frac{2}{3}II_\Omega]^3 \quad (A18)$$

and finally A'_3 is defined by

$$A'_3 = \frac{9}{5} + \frac{9}{4} C_{\text{Diff}} \max(1 + \beta_1^{(\text{eq})} II_S; 0) \quad (A19)$$

The purpose of the latter term in A'_3 is to model the ignored diffusion of the anisotropy.³ The parameter $\beta_1^{(\text{eq})}$ is defined as

$$\beta_1^{(\text{eq})} = -\frac{6}{5} \left\{ N^{(\text{eq})} / [(N^{(\text{eq})})^2 - 2II_\Omega] \right\} \quad (A20)$$

where

$$N^{(\text{eq})} = 81/20, \quad C_{\text{Diff}} = 2.2 \quad (A21)$$

To facilitate practical implementation in general CFD solvers, the Reynolds-stress tensor is expressed using an effective eddy-viscosity formulation including a corrective extra-anisotropy tensor $a_{ij}^{(ex)}$

$$\overline{u'_i u'_j} = -\nu_T \left(\frac{\partial U_i}{\partial x_j} + \frac{\partial U_j}{\partial x_i} \right) + \frac{2}{3} k \delta_{ij} + a_{ij}^{(ex)} k \quad (A22)$$

in which the effective eddy viscosity is defined as

$$\nu_T = (C_\mu / \beta^*) (k / \omega) = C_\mu k \tau, \quad C_\mu = -\frac{1}{2} (\beta_1 + II_\Omega \beta_6) \quad (A23)$$

$$\begin{aligned} a_{ij}^{(ex)} = & \beta_3 (\Omega_{ik}^* \Omega_{kj}^* - \frac{1}{3} II_\Omega \delta_{ij}) + \beta_4 (S_{ik} \Omega_{kj}^* - \Omega_{ik}^* S_{kj}) \\ & + \beta_6 (S_{ik} \Omega_{kl}^* \Omega_{lj}^* + \Omega_{ik}^* \Omega_{kl}^* S_{lj} - II_\Omega S_{ij} - \frac{2}{3} IV \delta_{ij}) \\ & + \beta_9 (\Omega_{ik}^* S_{kl} \Omega_{lm}^* \Omega_{mj}^* - \Omega_{ik}^* \Omega_{kl}^* S_{lm} \Omega_{mj}^*) \end{aligned} \quad (A24)$$

Acknowledgments

Part of this work was carried out within the HiAer Project (High Level Modelling of High Lift Aerodynamics, 2001–2004). The HiAer project was a collaboration of DLR, ONERA, Royal Institute of Technology in Sweden, Helsinki University of Technology, Technical University of Berlin, Alenia, EADS Airbus, QinetiQ, and Swedish Defence Research Agency (FOI). The project was managed by FOI and partly funded by the European Union (Project Reference: G4RD-CT-2001-00448). This work was also supported by the National Technology Agency of Finland (Tekes). The support from the European Union and Tekes is gratefully acknowledged.

References

- Durbin, P. A., "Separated Flow Computations with the $k-\varepsilon-v^2$ Model," *AIAA Journal*, Vol. 33, No. 4, 1995, pp. 659–664.
- Menter, F., "Two-Equation Eddy-Viscosity Turbulence Models for Engineering Applications," *AIAA Journal*, Vol. 32, No. 8, 1994, pp. 1598–1605.
- Wallin, S., and Johansson, A., "An Explicit Algebraic Reynolds Stress Model for Incompressible and Compressible Turbulent Flows," *Journal of Fluid Mechanics*, Vol. 403, Jan. 2000, pp. 89–132.
- Malone, M., "Extension of a $k-\omega$ Two-Equation Turbulence Model to an Algebraic Reynolds Stress Model," AIAA Paper 98-2552, June 1998.
- Lorentzen, L., and Lindblad, I., "Application of Two-Equation and EARSM Turbulence Models to High-Lift Aerodynamics," AIAA Paper 99-3181, June–July 1999.
- Hellsten, A., and Laine, S., "Explicit Algebraic Reynolds-Stress Modelling in Decelerating and Separating Flows," AIAA Paper 2000-2313, June 2000.
- Spalart, P., and Allmaras, S., "A One-Equation Turbulence Model for Aerodynamic Flows," *La Recherche Aéronautique*, No. 1, 1994, pp. 5–21.
- Cazalbou, J. B., Spalart, P., and Bradshaw, P., "On the Behavior of Two-Equation Models at the Edge of a Turbulent Region," *Physics of Fluids*, Vol. 6, No. 5, 1994, pp. 1797–1804.
- Catris, S., and Aupoix, B., "Towards a Calibration of the Length-Scale Equation," *International Journal of Heat and Fluid Flow*, Vol. 21, No. 5, 2000, pp. 606–613.
- Kok, J., "Resolving the Dependence on Freestream Values for the $k-\omega$ Turbulence Model," *AIAA Journal*, Vol. 38, No. 7, 2000, pp. 1292–1295.
- Hellsten, A., "New Two-Equation Turbulence Model for Aerodynamics Applications," Ph.D. Dissertation, Helsinki Univ. of Technology, Espoo, Finland, Feb. 2004, URL: <http://lib.hut.fi/Diss/>.
- Hellsten, A., and Bézard, H., "Behaviour of Nonlinear Two-Equation Turbulence Models at the Free-Stream Edges of Turbulent Flows," *Engineering Turbulence Modelling and Experiments* 6, Elsevier, 2005, pp. 147–156.
- Cazalbou, J.-B., and Chassaing, P., "The Structure of the Solution Edges of Turbulent Flows," *Physics of Fluids*, Vol. 14, No. 2, 2002, pp. 597–611.
- Wilcox, D., "Reassessment of the Scale-Determining Equation for Advanced Turbulence Models," *AIAA Journal*, Vol. 26, No. 11, 1988, pp. 1299–1310.
- Wilcox, D., *Turbulence Modeling for CFD*, 2nd ed. DCW Industries, Inc., La Canada, CA, 1998.
- Driver, D., "Reynolds Shear Stress Measurements in a Separated Boundary Layer Flow," AIAA Paper 91-1787, June 1991.
- Moir, I., "Measurements on a Two-Dimensional Aerofoil with High-Lift Devices," AGARD AR-303, Vol. 2, 1994, pp. A2.1–A2.12.
- Menter, F., "Influence of Freestream Values on $k-\omega$ Turbulence Model Predictions," *AIAA Journal*, Vol. 30, No. 6, 1992, pp. 1657–1659.
- Klebanoff, P., "Characteristics of Turbulence in a Boundary Layer with Zero Pressure Gradient," NACA, Rept. 1247, 1955.
- Wiegardt, K., and Tillman, W., "On the Turbulent Friction Layer for Rising Pressure," NACA TM 1314, July 1951.
- Winter, K., and Gaudet, L., "Turbulent Boundary-Layer Studies at High Reynolds Number at Mach Numbers Between 0.2 and 2.8," Aeronautical Research Council, Rept. ARC R&M 3712, London, 1973.
- Townsend, A., "The Fully Developed Turbulent Wake of a Circular Cylinder," *Australian Journal of Scientific Research*, Vol. 2, No. 4, 1949, pp. 451–468.
- Thomas, R., "Conditional Sampling and Other Measurements in a Plane Turbulent Wake," *Journal of Fluid Mechanics*, Vol. 57, No. 3, 1973, pp. 549–582.
- Fabris, G., "Conditional Sampling Study of the Turbulent Wake of a Cylinder. Part 1," *Journal of Fluid Mechanics*, Vol. 94, No. 4, 1979, pp. 673–709.
- Antonia, R., and Browne, L., "Anisotropy of the Temperature Dissipation in a Turbulent Wake," *Journal of Fluid Mechanics*, Vol. 163, 1986, pp. 393–403.
- Weygant, J., and Mehta, R., "Three-Dimensional Structure of Straight and Curved Plane Wakes," *Journal of Fluid Mechanics*, Vol. 282, 1995, pp. 279–311.
- Liepmann, H., and Laufer, J., "Investigations of Free Turbulent Mixing," NACA TN 1257, Aug. 1947.
- Castro, I., and Bradshaw, P., "The Turbulence Structure of a Highly Curved Mixing Layer," *Journal of Fluid Mechanics*, Vol. 73, No. 2, 1976, pp. 265–304.
- Wynanski, I., and Fiedler, H., "The Two-Dimensional Mixing Region," *Journal of Fluid Mechanics*, Vol. 41, No. 2, 1970, pp. 327–361.
- Hanjalic, K., and Launder, B. E., "A Reynolds Stress Model of Turbulence and Its Application to Thin Shear Flows," *Journal of Fluid Mechanics*, Vol. 52, No. 4, 1972, pp. 609–638.

- ³¹Launder, B. E., Reece, G. J., and Rodi, W., "Progress in the Development of a Reynolds-Stress Turbulence Closure," *Journal of Fluid Mechanics*, Vol. 68, No. 3, 1975, pp. 537–566.
- ³²Siikonen, T., "An Application of Roe's Flux-Difference Splitting for the $k-\epsilon$ Turbulence Model," *International Journal for Numerical Methods in Fluids*, Vol. 21, No. 11, 1995, pp. 1017–1039.
- ³³Kaurinkoski, P., and Hellsten, A., "FINFLO: the Parallel Multi-Block Flow Solver," Lab. of Aerodynamics, Helsinki Univ. of Technology, Rept. A-17, Espoo, Finland, Jan. 1998.
- ³⁴Clauser, F., "Turbulent Boundary Layers in Adverse Pressure Gradients," *Journal of Aeronautical Sciences*, Vol. 21, 1954, pp. 91–108.
- ³⁵Coles, D., and Hirst, E. (eds), *Computation of Turbulent Boundary Layers—1968 AFOSR-IFP-Stanford Conference*, Vol. 2, Stanford Univ., Stanford, CA, 1969, pp. 210–221.
- ³⁶Skåre, P., and Krogstad, P., "A Turbulent Equilibrium Boundary Layer near Separation," *Journal of Fluid Mechanics*, Vol. 272, 1994, pp. 319–348.
- ³⁷Launder, B. E., and Spalding, D., "The Numerical Computation of Turbulent Flows," *Computer Methods in Applied Mechanics and Engineering*, Vol. 3, 1974, pp. 269–289.
- ³⁸Rodi, W., and Scheuerer, G., "Scrutinizing the $k-\epsilon$ Turbulence Model Under Adverse Pressure Gradient Conditions," *Journal of Fluids Engineering*, Vol. 108, June 1986, pp. 174–179.
- ³⁹Gullman-Strand, J., Amberg, G., and Johansson, A., "Numerical Study of Separated Flow in a Plane Asymmetric Diffuser," *Third International Symposium on Turbulence and Shear Flow Phenomena*, edited by N. Kasagi, J. K. Eaton, R. Friedrich, J. A. C. Humphrey, M. A. Leschziner, and T. Miyauchi, Vol. 1, 2003, pp. 251–256.
- ⁴⁰Gullman-Strand, J., "Turbulence and Scalar Flux Modelling Applied to Separated Flows," Ph.D. Dissertation, Dept. of Mechanics, Royal Inst. of Technology, Stockholm, Dec. 2004.
- ⁴¹Hellsten, A., "On the Solid-Wall Boundary Condition of ω in the $k-\omega$ Type Turbulence Models," Lab. of Aerodynamics, Helsinki Univ. of Technology, Rept. B-50, Espoo, Finland, March 1998.
- ⁴²Thivet, F., Daouk, M., and Knight, D., "Influence of the Wall Condition on $k-\omega$ Turbulence Model Predictions," *AIAA Journal*, Vol. 40, No. 1, 2002, pp. 179–181.
- ⁴³Gendre, P., "Maximum Lift for Single-Element Airfoils—Experimental Results A—Airfoil," *EUROVAL—A European Initiative on Validation of CFD Codes*, Vol. 42, Notes on Numerical Fluid Mechanics, edited by W. Haase, F. Brandsma, E. Elsholz, M. Leschziner, and D. E. Schwaborn, Vieweg Verlag, Braunschweig, Germany, 1992.
- ⁴⁴Coles, D., and Wadcock, A., "Flying-Hot-Wire Study of Flow past an NACA 4412 Airfoil at Maximum Lift," *AIAA Journal*, Vol. 17, No. 4, 1979, pp. 321–329.
- ⁴⁵Fejtek, I., "Summary of Code Validation Results for a Multiple Element Airfoil Test Case," AIAA Paper 97-1932, June–July 1997.
- ⁴⁶Rumsey, C., Gatski, T., Ying, S., and Bertelrud, A., "Prediction of High-Lift Flows Using Turbulent Closure Models," AIAA Paper 97-2260, June 1997; also *AIAA Journal*, Vol. 36, No. 5, 1998, pp. 765–774.
- ⁴⁷Rudnik, R., "Untersuchung der Leistungsfähigkeit von Zweigleichungs-Turbulenzmodellen bei Profilumströmungen," Ph.D. Dissertation, Technische Univ. Berlin, DLR Forschungsbericht 97-49, Cologne, Germany, Sept. 1997.
- ⁴⁸Wild, J., "Numerische Optimierung von Zweidimensionalen Hochauftriebskonfigurationen durch Lösung der Navier-Stokes-Gleichungen," Ph.D. Dissertation, Technische Univ. Carolo-Wilhelmina zu Braunschweig, DLR Forschungsbericht 2001-11, Cologne, Germany, June 2001.
- ⁴⁹Wallin, S., and Johansson, A., "Modelling Streamline Curvature Effects in Explicit Algebraic Reynolds Stress Turbulence Models," *International Journal of Heat and Fluid Flow*, Vol. 23, No. 5, 2002, pp. 721–730.
- ⁵⁰Hellsten, A., Wallin, S., and Laine, S., "Scrutinizing Curvature Corrections for Algebraic Reynolds Stress Models," AIAA Paper 2002-2963, June 2002.
- ⁵¹Wallin, S., Hellsten, A., Schatz, M., Rung, T., Peshkin, D., and Johansson, A., "Streamline Curvature Corrected Algebraic Reynolds Stress Turbulence Modelling," *Third International Symposium on Turbulence and Shear Flow Phenomena*, edited by N. Kasagi, J. K. Eaton, R. Friedrich, J. A. C. Humphrey, M. A. Leschziner, and T. Miyauchi, Vol. 1, 2003, pp. 45–50.
- ⁵²Hellsten, A., "New Advanced $k-\omega$ Turbulence Model for High-Lift Aerodynamics," AIAA Paper 2004-1120, Jan. 2004.

P. Givi
Associate Editor